Nano Research

Open Access

Research Article

Highly anisotropic dual-heterostructure for multifunctional solar-blind polarization-sensitive photodetectors

Qian Li[1,§], Kun Ye[3,§], Mengmeng Yang[1] ✉, Junxin Yan[4], Tianle Zeng[4], Qi Gao[5], Yang Lv[3], Yihan Gao[3], Qingqing Yang[1], Ruiqi Chen[1], Yang Gao[1], Zhaofei Sun[1], Bo He[1], Peng Xiao[2], Wei Ye[2] ✉, Anmin Nie[4], Zhongyuan Liu[4], and Shouguo Wang[1] ✉

[1] *Anhui Provincial Key Laboratory of Magnetic Functional Materials and Devices, Faculty of Materials Science and Engineering, Anhui University, Hefei 230601, China*
[2] *School of Information Engineering, Nanchang Hangkong University, Nanchang 330063, China*
[3] *School of Electronics and Information Engineering, Institute of Quantum Materials and Devices, State Key Laboratory of Separation Membrane and Membrane Processes, Tiangong University, Tianjin 300387, China*
[4] *Center for High Pressure Science (CHiPS), State Key Laboratory of Metastable Materials Science & Technology, Yanshan University, Qinhuangdao 066004, China*
[5] *School of Materials Engineering, Shanxi College of Technology, Shuozhou 036000, China*
§ *Qian Li and Kun Ye contributed equally to this work.*

Cite this article: *Nano Research*, **2026**, *19*, 94908448. https://doi.org/10.26599/NR.2026.94908448

ABSTRACT: Solar-blind ultraviolet photodetectors based on two-dimensional van der Waals heterostructures have emerged as indispensable components for high-precision warning systems, environmental monitoring systems, information encryption, and optical communication. However, the widespread use of solar-blind ultraviolet photodetectors is still constrained by the simultaneous lack of ultralow dark current, high specific photoresponse, sub-microsecond response time, and intrinsic polarization-sensitive photoresponse. Herein, a dual-heterostructure field-effect transistor composed of the ultra-wide bandgap semiconductor $GaPS_4$ and WS_2 nanosheets was fabricated. The $WS_2/GaPS_4$ dual-heterostructure devices exhibit high spike barriers at the dual-heterostructure interface owing to type-I band alignment, which can completely suppress charge transfer. Furthermore, the device exhibits an outstanding performance in the solar-blind ultraviolet (UV) region, stemming from the fast carrier separation and transfer enabled by the built-in electric fields at the dual-heterostructure interface. Critically, the two-fold rotational symmetry (C_2) of $GaPS_4$ breaks the original three-fold rotational symmetry (C_3) of WS_2 to simultaneously achieve unexpected linearly polarized Raman and anisotropic absorptions at the heterostructure interface. Moreover, the $WS_2/GaPS_4$ dual-heterostructure photodetector possesses high-resolution polarization imaging capability under 255 nm illumination owing to dichroic ratios as high as 3.4. These results suggest that the novel two-dimensional dual-heterostructure provides a foundation for developing next-generation polarization-sensitive multifunctional photodetectors.

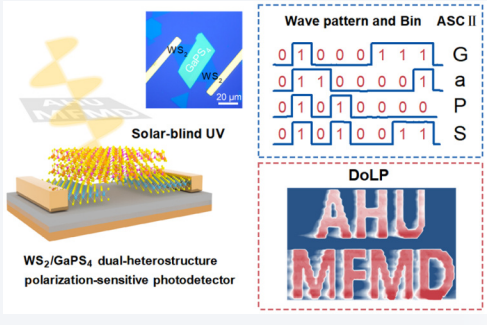

KEYWORDS: $WS_2/GaPS_4$ dual-heterostructure, type-I band alignment, anisotropic optical response, solar-blind ultraviolet photodetector, high-resolution polarization imaging

1 Introduction

Polarization-resolved solar-blind ultraviolet photodetectors (λ = 200–280 nm) have become indispensable in the fields of high-precision warning and tracking, environmental monitoring, secure optical communications, and flame detection [1–4]. State-of-the-art photodetectors in the solar-blind ultraviolet (UV) range including Ga_2O_3 [5], AlN [6], and diamond [7] are technologically mature but remain encumbered by high-temperature epitaxy, sophisticated technology integration, interface defects, and concomitant performance degradation [8]. Recently, low-symmetry ultra-wide bandgap semiconductors, such as $GaPS_4$ [9], KNb_3O_8 [10], Rb_2CuCl_3 [11], and $GaTe_{0.5}Se_{0.5}$ [12], have emerged as ideal charge-

Received: November 14, 2025; **Revised:** December 20, 2025
Accepted: January 15, 2026

✉Address correspondence to Mengmeng Yang, mmyangphy@ahu.edu.cn; Wei Ye, yeweinchu@126.com; Shouguo Wang, sgwang@ahu.edu.cn

trapping layers owing to their large absorption coefficients, high saturation electron velocity, excellent thermal conductivity, and robust thermal and chemical stability [13–17]. However, insufficient optical absorption, pronounced carrier recombination, and limited intrinsic anisotropy restrict the use of high-resolution polarization photodetectors in the solar-blind UV regions.

The atomic-level thickness of WS_2, a typical member of the transition metal chalcogenide (TMDC) family, results in an exceptional absorption coefficient and long carrier-diffusion length, making it attractive for high-performance photodetectors. The van der Waals (vdW) heterostructure band-alignment engineering further displays an atomically sharp interface, strong light–matter interactions, suppression of interfacial recombination, and ultrafast charge extraction [18–20]. Nevertheless, it remains challenging for two-dimensional heterostructure photodetectors to simultaneously exhibit the high dichroic ratios (DR), high photoresponsivity, ultralow dark current, and rapid responses. Consequently, dual-heterostructures and superlattices based on two-dimensional materials have been proposed to achieve high-performance multifunctional photodetectors [21–23]. Complete depletion of the intermediate absorbing layer in two parallel heterostructures not only reduces the transport distance of photocarriers but also significantly enhances the light absorption efficiency [22, 24]. Moreover, introducing a high electron barrier and large built-in electric field at the type-I dual-heterostructure interface ensures the rapid separation and transfer of photogenerated electron–hole pairs while effectively preventing the drift of minority carriers [25]. More importantly, the precisely engineered lattice mismatch at the dual interface breaks the intrinsic symmetry of the target material, giving rise to Moiré superlattices that substantially amplify the polarized electronic states. Consequently, synergistic band structure and symmetry engineering within wide-bandgap dual-heterostructures offer a potential pathway for realizing multifunctional solar-blind UV detectors with high performance and exceptional polarization sensitivity.

In this work, we constructed a novel vdW dual-heterostructure field effect transistor (FET) composed of a bottom monolayer WS_2 and middle multilayer $GaPS_4$. Comprehensive characterization techniques, including optical microscopy (OM), photoluminescence (PL), atomic force microscopy (AFM), Kelvin probe force microscopy (KPFM), and high-angle annular dark field scanning transmission electron microscopy (HAADF-STEM), were employed to evaluate the crystal quality. Ultrafast transient absorption (TA) spectroscopy and density functional theory (DFT) calculations were performed to elucidate the underlying carrier transport mechanisms in the $WS_2/GaPS_4$ dual-heterostructure. Interestingly, two unique built-in electric fields were constructed at the dual-heterostructure interface, facilitating the efficient and rapid separation and transfer of photogenerated carriers. The device based on the $WS_2/GaPS_4$ dual-heterostructure exhibits a low dark current, fast response time, and high dichroic ratio. Furthermore, this dual-heterostructure photodetector enables encoded optical communication and high-resolution polarization imaging. Our findings provide a promising route for developing high-performance and polarization-sensitive photodetectors in the solar-blind UV region based on two-dimensional dual-heterostructures.

2 Experimental

2.1 Preparation of $GaPS_4$ crystal and WS_2 nanosheets

High quality bulk $GaPS_4$ crystals were prepared by the chemical vapor transport (CVT) method. Firstly, a mixture of gallium (Ga), phosphorus (P), and sulfur (S) powders with a molar ratio of 1:1:4 was loaded into a quartz tube. Subsequently, the temperature was gradually ramped up to 750 °C, held for one week, and finally was naturally cooled to room temperature to obtain $GaPS_4$ crystals. WS_2 nanosheets were synthesized by the chemical vapor deposition (CVD) method in tube furnace. The precursor S powder was placed in the center of the low temperature zone, while the WO_3 powder and substrate were placed in the center of the high temperature zone. The temperatures of the low and high temperature zones were simultaneously increased to 260 and 920 °C, respectively, within 30 min, maintained for 25 min, and then was naturally cooled to room temperature. WS_2 nanosheets were successfully obtained on the SiO_2/Si substrate.

2.2 Heterostructure fabrication

The vdW $WS_2/GaPS_4$ dual-heterostructure was fabricated via an accurate transfer platform (Metatest, E1-G). The schematic diagram of the heterostructure fabrication process is displayed in Fig. S3 in the Electronic Supplementary Material (ESM). Multilayer $GaPS_4$ nanosheets were mechanically exfoliated from bulk $GaPS_4$ crystal using transparent tape. Next, a suitable $GaPS_4$ nanosheet was selected and was precisely transferred onto an adjacent monolayer WS_2 nanosheets on SiO_2/Si substrate. Finally, the $WS_2/GaPS_4$ dual-heterostructure was heated at 80 °C for 10 min on a hot plate to enhance the interaction between the sample and substrate. Details regarding the STEM sample preparation are provided in Note S2 in the ESM.

2.3 Sample characterizations

The morphology of $WS_2/GaPS_4$ dual-heterostructure was characterized by using OM (D4000M, Leica) and AFM (multimode 8, Bruker). Raman and PL spectroscopy of the $WS_2/GaPS_4$ heterostructure were investigated by a confocal Raman spectrometer (JY Horiba, HR Evolution). The phase structure, elemental composition, and valence states were analyzed by STEM (Talos F200X, Thermo Fisher) and X-ray photoelectron spectroscopy (XPS; ESCALAB 250Xi, Thermo Fisher Scientific). The micro-area UV–visible–near infrared (UV–Vis–NIR) absorption spectra were collected by a confocal spectrometer in the transmission mode (MStarter ABS, Metatest). The TA spectra were collected by using an integrated Helios setup (Ultrafast Systems). Femtosecond laser pulses were generated by a Ti:Sapphire amplifier at a repetition rate of 1 kHz (Spectra-Physics Solstice Ace). The 800 nm fundamental passed through a beam splitter, where most of the beam was sent into an optical parametric amplifier (Ultrafast Systems, Apollo-T) to generate 400 and 267 nm pulses for the pump. The rest of the fundamental was focused into a Vis continuum-generation crystal (Ultrafast, Helios) to generate the white-light continuum.

2.4 Device fabrication and measurements

The $WS_2/GaPS_4$ dual-heterostructure devices were fabricated through a series of processes including laser direct writing lithography, metal thermal evaporation, and lift-off processes. The electrical and optoelectronic luminated data were recorded using Keithley 2634B dual source meter. The optoelectrical measurement of $WS_2/GaPS_4$ dual-heterostructure photodetector was conducted using the metatest scanpro laser scanning system (ScanPro Advance, Metatest) with a wavelength-adjustable light-emitting

diode (LED) (255–1550 nm) as the light source. Time-resolved photo-response data were collected with a lock-in amplifier (Dlpca200, Femto) equipped with an optical chopper. The degree of linear polarization (DoLP) can be calculated by using the following equations

$$S_0 = I_{0^\circ}(x, y) + I_{90^\circ}(x, y) \quad (1)$$

$$S_1 = I_{0^\circ}(x, y) - I_{90^\circ}(x, y) \quad (2)$$

$$S_2 = I_{45^\circ}(x, y) - I_{135^\circ}(x, y) \quad (3)$$

$$\mathrm{DoLP} = \frac{\sqrt{S_1^2 + S_2^2}}{S_0} \quad (4)$$

where S_0, S_1, and S_2 represent the total intensity, the first Stokes parameter, and the second Stokes parameter, respectively. $I_{0^\circ}(x, y)$, $I_{45^\circ}(x, y)$, $I_{90^\circ}(x, y)$, and $I_{135^\circ}(x, y)$ denote the intensity images acquired through linear polarizers oriented at 0°, 45°, 90°, and 135°, respectively, where (x, y) indicates the spatial coordinates in the image plane.

2.5 DFT calculation

First-principles calculations were performed using the projector-augmented wave (PAW) method, as implemented within the Vienna *ab-initio* simulation package (VASP). The exchange-correlation interactions were modeled using the Perdew–Burke–Ernzerhof (PBE) functional, which is situated within the generalized gradient approximation (GGA) paradigm. To account for vdW interactions, Grimme's DFT-D3 approach was adopted. To mitigate artificial interactions between neighboring images in the simulations of two-dimensional and few-layer $WS_2/GaPS_4$ structures, a vacuum spacing of 15 Å was introduced along the *z*-axis. After conducting a series of convergence studies, an energy cutoff of 650 eV was selected for the plane waves, and the first Brillouin zone was sampled using a Monkhorst–Pack *k*-point mesh with a spacing of $2\pi \times 0.03$ Å^{-1}. The structural relaxation process was concluded when both the total energy changes and the ionic Hellmann–Feynman forces fell below stringent thresholds of 5.0×10^{-6} V and 0.01 eV/Å, respectively.

3 Results and discussion

Schematics of the crystal model and an optical image of the $WS_2/GaPS_4$ dual-heterostructure are shown in Fig. 1(a). A typical $WS_2/GaPS_4$ dual-heterostructure is fabricated with $GaPS_4$ nanosheets bridging two neighbouring monolayer WS_2 nanosheets. Further details on the experimental growth and transfer exfoliation processes are presented in Section 2 and Figs. S1–S4 in the ESM. The optical image, AFM image, and corresponding height profiles of pure $GaPS_4$ nanosheets (Fig. S5 in the ESM) highlight the features of a typical layered crystal structure. Figures 1(b) and 1(c) show the Raman and PL spectra of the individual WS_2, $WS_2/GaPS_4$, and $GaPS_4$ heterostructure regions. In the WS_2 region, the major Raman peaks at 175, 230 296, 323, 351, 355, and 419 cm^{-1} belong to the LA(M), A1(M)-LA(M), E″(G), E″(M), 2LA(M), E′(G), and A_{1g} vibration modes, respectively, which is consistent with previously obtained results [26]. For the heterostructure region, eight additional peaks, A_g^1 (71.9 cm^{-1}), A_g^2 (81.6 cm^{-1}), A_g^3 (110.6 cm^{-1}), B_g (119.8cm^{-1}), A_g^4 (149.3 cm^{-1}), A_g^5 (189.8 cm^{-1}), A_g^6 (381.4 cm^{-1}), and A_g^7 (427.7 cm^{-1}), are attributed to the Raman peak vibrational modes of $GaPS_4$ nanosheets [9]. The PL spectrum (Fig. 1(c)) shows a strong emission peak located at 1.96 eV, indicative of the direct bandgap of monolayer WS_2 [26]. However, the $WS_2/GaPS_4$ heterostructure shows a significant PL quenching effect and the peak is red-shifted, suggesting efficient separation and transfer of the photogenerated electron–hole pairs [27]. The thickness-dependence of the Raman and PL intensities of the $WS_2/GaPS_4$ heterostructure is shown in Fig. S6 in the ESM. The uniform Raman and PL intensity mappings (Fig. S7 in the ESM) further confirm the high quality of as-prepared $WS_2/GaPS_4$ heterostructure. The absorption spectra of WS_2, $WS_2/GaPS_4$, and $GaPS_4$ are shown in Fig. 1(d). The blue arrows located at 617, 514, and 427 nm belong to the A, B, and C excitons of pure WS_2, respectively, while the red arrow at 265 nm is attributed to the exciton peak of $GaPS_4$, which is consistent with a previous report [9]. Notably, within the overlapping region of the heterojunction, the absorption is dramatically enhanced in the solar-blind UV region, implying the potential for high-performance solar-blind photodetection. The chemical composition and atomic-scale stacking structure of the dual-heterostructure were further investigated by aberration-corrected STEM (Ac-STEM). The HAADF images and elemental mapping (Fig. S8 in the ESM) show a uniform distribution of Ga, P, S, and W, indicating the high-quality stacking structure of the $WS_2/GaPS_4$ heterostructure. The selected area electron diffraction (SAED) pattern (Fig. 1(e)) reveals two sets of diffraction spots, corresponding to the hexagonal monolayer WS_2 and monoclinic $GaPS_4$ crystal, with an orientation relationship of $GaPS_4$ [201]//WS_2[001], as verified by X-ray diffraction (XRD) and SAED. The atomic-scale HAADF-STEM image (Fig. 1(f)) of the $WS_2/GaPS_4$ heterostructure shows a lattice spacing of 0.76 nm, assigning to the $(20\bar{4})$ plane of the $GaPS_4$ crystal. Figure S9 in the ESM shows XPS spectra, confirming the binding energies of W 4f, Ga 2p, P 2p, and S 2p, which agree with those previously reported [9, 27]. Figures 1(g) and 1(h) exhibit an AFM image and the corresponding KPFM image, respectively. The corresponding height profiles (Fig. 1(i), top) indicate the thicknesses of 0.7 nm for WS_2 and 20.3 nm for $GaPS_4$, while the surface potential of the $GaPS_4$ in the middle region is higher than that of the WS_2 and the difference is calculated to be 106 mV (Fig. 1(i), bottom). Notably, two distinct spike-shaped surface potential features are clearly observed in the $WS_2/GaPS_4$ dual-heterostructure region, implying the formation of a larger built-in potential at the $WS_2/GaPS_4$ interface. The thickness-dependent work function of $GaPS_4$ suggests the possibility of tuning the barrier height by controlling the number of layers (Fig. S10 in the ESM).

Ultrafast TA spectroscopy and DFT calculations were employed to further investigate the electron–hole pair transfer between WS_2 and $GaPS_4$. The real-time photoexcited exciton dynamics within WS_2 and the $WS_2/GaPS_4$ heterostructure are directly monitored by TA spectroscopy using pump pulses lasers at 267 and 400 nm (a detailed schematic of the femtosecond TA experimental setup is shown in Fig. S11 in the ESM). As depicted in Figs. 2(a) and 2(b), the TA spectra of pristine WS_2 pumped at 267 nm exhibits two negative signals located at 617 and 514 nm of the ground state bleach (GSB), corresponding to the A and B excitons of WS_2 [28], respectively. A 400 nm pump pulse laser is chosen to selectively excite WS_2 while keeping $GaPS_4$ in an unexcited state. The GSB signal intensity of A and B excitons in the heterostructure region is significantly weaker than those observed for pristine WS_2, as shown

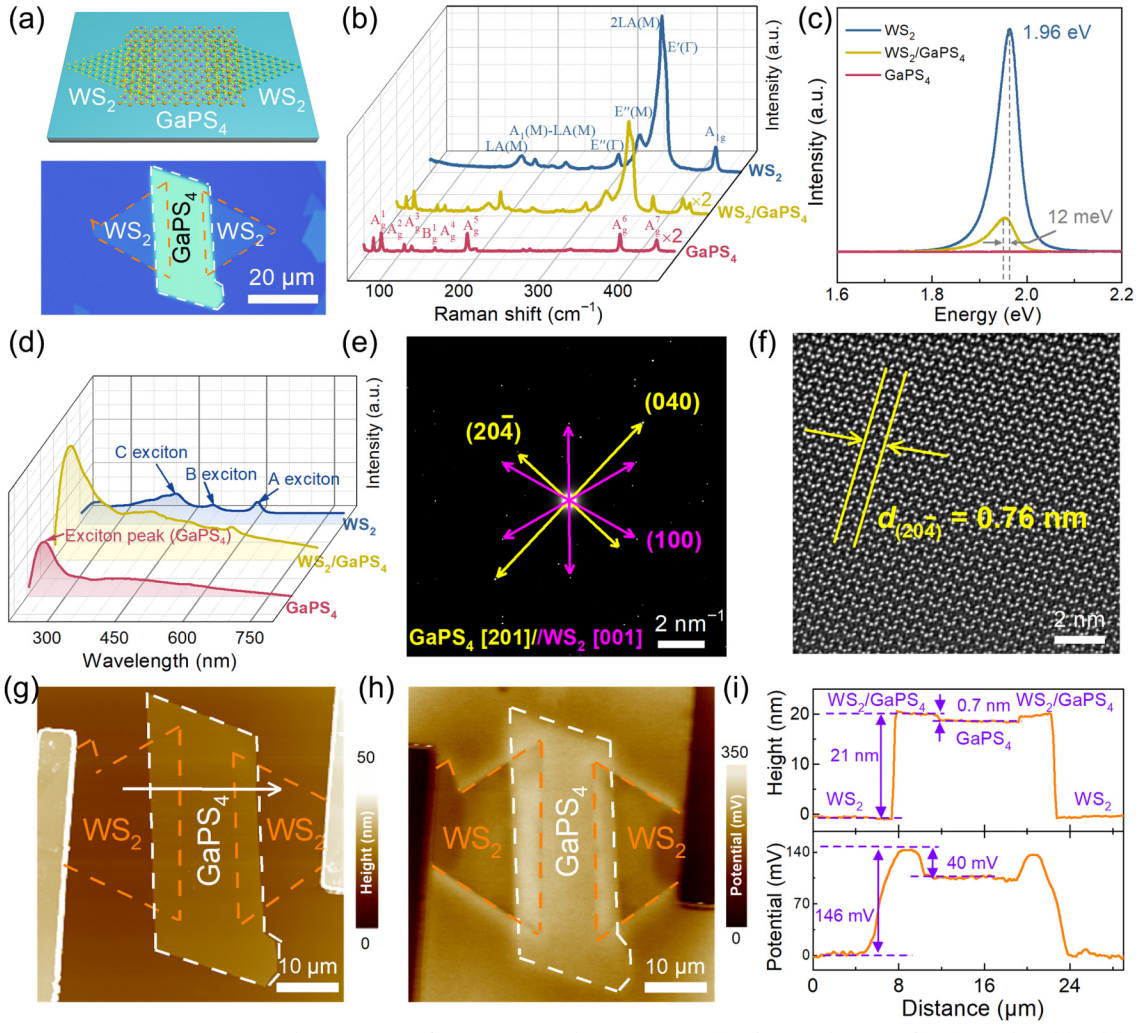

Figure 1 OM, Raman, PL, TEM, AFM, KPFM characterization of $WS_2/GaPS_4/WS_2$ heterostructures. (a) Schematic diagrams of (top) crystal model and (bottom) optical microscopy image for $WS_2/GaPS_4$ dual-heterostructure fabricated on the SiO_2/Si substrate. The $GaPS_4$ layer is located at top of two adjacent monolayer WS_2 nanosheets. ((b) and (c)) Raman and PL spectra collected from WS_2, $WS_2/GaPS_4$, and $GaPS_4$ under 532 nm laser excitation. The LA(M), A1(M)-LA(M), E″(Γ), E″(M), 2LA(M), E′(Γ), and A_{1g} vibrational peaks are attributed to WS_2, whereas the A_g^1, A_g^2, A_g^3, B_g, A_g^4, A_g^5, A_g^6, and A_g^7 are attributed to $GaPS_4$. The PL peak of the pure monolayer WS_2 is located at 1.96 eV, whereas the PL peaks in the heterostructure region are greatly diminished and shifted, indicating efficient photogenerated electron–hole pairs separation and transfer. (d) The absorption spectra of WS_2, $WS_2/GaPS_4$, and $GaPS_4$. The bule arrow marks located at 617, 514, and 427 nm belong to A exciton, B exciton, and C exciton of pure WS_2, respectively. The red arrow mark located at 265 nm is attributed to the exciton peak of $GaPS_4$. ((e) and (f)) The SADE pattern and corresponding HADDF-STEM image of $WS_2/GaPS_4$ heterostructure. ((g) and (h)) Typical AFM and KPFM images of $WS_2/GaPS_4$ dual-heterostructure, respectively. From the center to the sides: $GaPS_4$, $WS_2/GaPS_4$, WS_2, and Au. (i) (top) The corresponding height profiles and (bottom) the surface potential difference $WS_2/GaPS_4$ dual-heterostructure.

in Fig. S12 in the ESM. Conversely, the GSB signal intensity for A and B excitons pumped by 267 nm in the heterostructure region exhibits markedly higher intensities than that of pristine WS_2, providing unambiguous evidence that electrons and holes photogenerated in $GaPS_4$ are quantitatively transferred into the WS_2 layer. In addition, the TA spectra recorded 1 ps after 267 nm photoexcitation (Fig. 2(c)) show state-filling in $GaPS_4$, driven by fast electron–hole injection from $GaPS_4$ into WS_2. DFT calculations are used to explain the charge transfer mechanism between WS_2 and $GaPS_4$.

Figure 2(d) presents the electronic band structure of the $WS_2/GaPS_4$ heterostructure. The valence band maximum (VBM) is primarily composed of W and S atoms from WS_2, whereas the conduction band minimum (CBM) consists mainly of the Ga and S atoms from $GaPS_4$, with minor contributions from P atoms (Fig. 2(e)), suggesting that the orbital hybridization predominantly occurs in the non-band-edge region [29]. Moreover, the CBM of the WS_2 is lower than that of the $GaPS_4$, whereas the VBM of WS_2 is higher than that of $GaPS_4$, confirming the type-I band alignment (Fig. 2(f)), which is consistent with the TA observations.

Moreover, the symmetry engineering strategy, achieved by incorporating $GaPS_4$ (C_2 symmetry) into monolayer WS_2 (C_3 symmetry), triggers pronounced interfacial effects of orbital hybridization and uniaxial lattice distortion, which breaks the intrinsic C_3-symmetric lattice of pristine WS_2 [27]. Angle-resolved polarization Raman spectroscopy (ARPRS) and angle-resolved polarization absorption spectroscopy (ARPAS) further reveal a markedly enhanced anisotropic optical response at the $WS_2/GaPS_4$ dual-heterostructure interface. Figure 3(a) illustrates the experimental geometry of the ARPRS results in parallel and cross configurations. Owing to the C_3 rotational symmetry of pristine WS_2, the Raman-active modes exhibit isotropic intensity

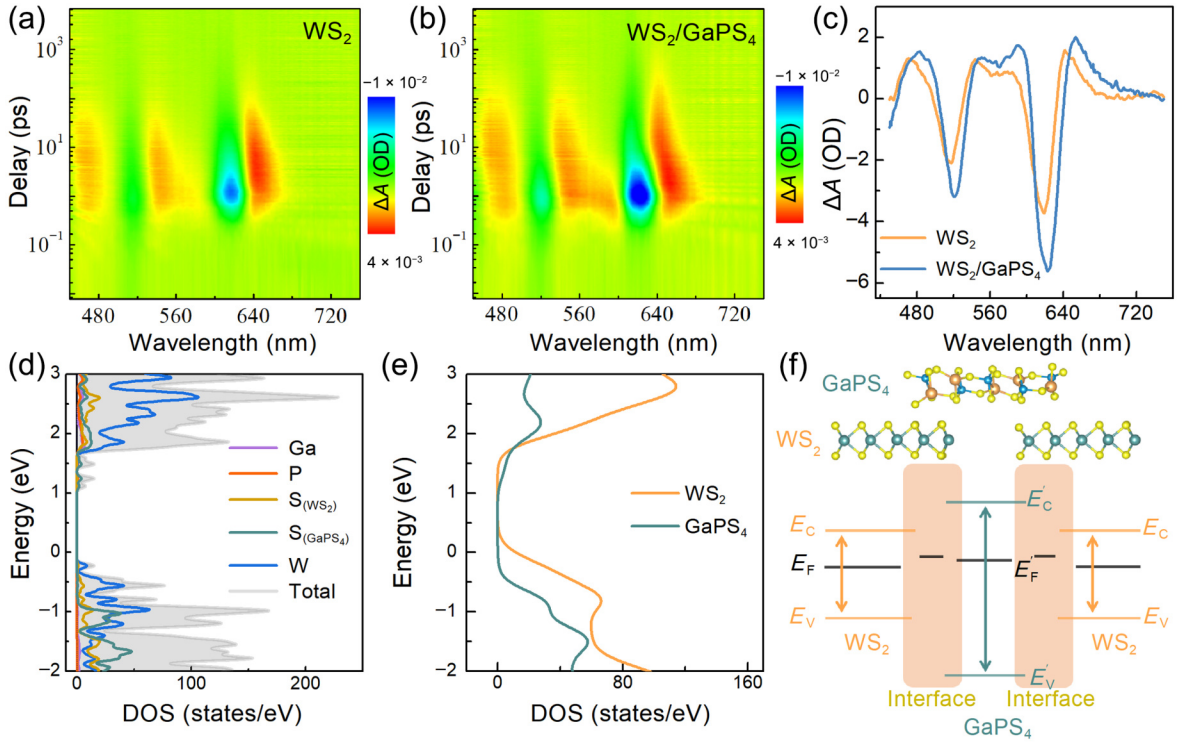

Figure 2 Transient absorption spectroscopy characterization and theoretical calculation of $WS_2/GaPS_4$ dual-heterostructure. ((a) and (b)) Pristine WS_2 and $WS_2/GaPS_4$ heterostructures under 267 nm pump pulses laser. (c) TA spectra extracted from the mappings in ((a) and (b)) WS_2 and $WS_2/GaPS_4$ heterostructures at 1 ps delay time. (d) Partial density of states (PDOS) based on Ga, P, S(WS_2), S($GaPS_4$) and W atoms. (e) DOS projected to $GaPS_4$ and WS_2. (f) Band alignment of $WS_2/GaPS_4$ dual-heterostructure before contact.

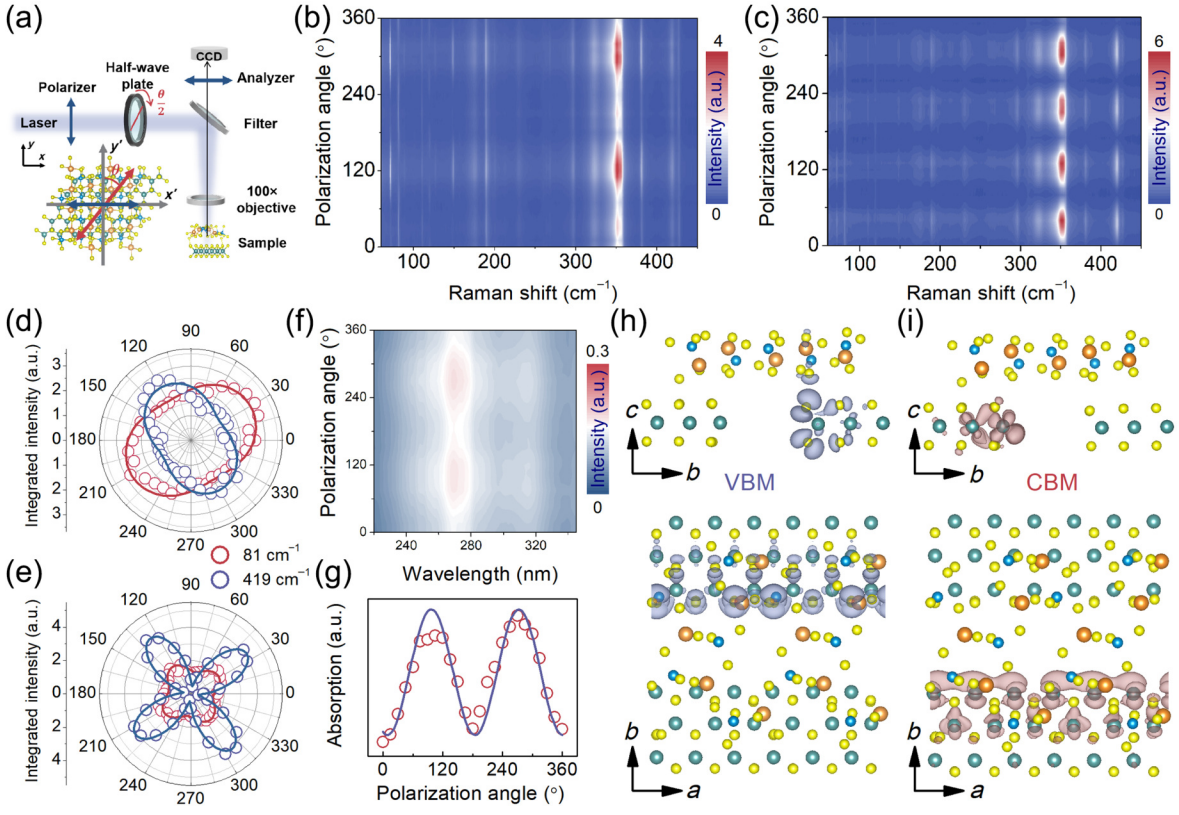

Figure 3 Anisotropic optical response of $WS_2/GaPS_4$ heterostructure interface. (a) Schematic diagrams of the angle-resolved polarized Raman spectroscopy. (b) and (c) Polarized Raman intensity mappings of $WS_2/GaPS_4$ heterostructure under parallel and cross configurations. (d) and (e) Polar plots of the measured and fitted peak intensities under parallel and cross configuration based on $WS_2/GaPS_4$ heterostructure in 81 and 419 cm^{-1}. (f) and (g) Contour mapping and extracted 267 nm exciton peak of ARPRS under parallel configurations. (h) and (i) The spatial distributions of the VBM and CBM wave functions in the *bc*- and *ab*-planes.

distributions as the polarization angle changed [27]. Figures 3(b) and 3(c) display the contour mapping of angle-dependent Raman intensity under parallel and cross configurations for $WS_2/GaPS_4$ heterostructure. By introducing the low-symmetry $GaPS_4$ layer (C_2 symmetry), the interfacial interaction breaks the three-fold symmetry of WS_2, rendering the Raman modes linearly polarized. Remarkably, the Raman characteristic peaks of $WS_2/GaPS_4$ heterostructure region display identical periodicities of π and π/2 (Figs. 3(d) and 3(e)), providing the evidence that the symmetry of WS_2 is effectively re-engineered by the adjacent $GaPS_4$ through tunable interlayer coupling. Detailed quantitative analyses are provided in Fig. S13 and Note S1 in the ESM. Similar results are observed in the ARPAS (Figs. 3(f) and 3(g)). The excitonic peak of $GaPS_4$ at 267 nm is significantly enhanced by the incorporation of WS_2 and exhibits π-periodic oscillations with polarization angle, indicating potential application solar-blind UV polarization photodetector. Moreover, the partial charge density (PCD) was calculated to evaluate the electron density distribution at the $WS_2/GaPS_4$ dual-heterostructure interface. The spatial distributions of the VBM (Fig. 3(h)) and CBM (Fig. 3(i)) wave functions show clear distinctions between the *ab*- and *bc*-planes, suggesting the intrinsic in-plane anisotropic optical response. Notably, the asymmetrical and non-uniform charge density distribution at the dual-heterostructure interfaces effectively promotes the anisotropic charge separation in the built-in electric field, significantly enhancing the in-plane optical anisotropy of $WS_2/GaPS_4$ dual-heterostructure.

To investigate the optoelectronic properties of $WS_2/GaPS_4$ dual-heterostructure, a back-gate FET was fabricated on SiO_2/Si substrate (Fig. 4(a)). The transfer characteristics curve (Fig. 4(b)) reveals typically n-type conductive behavior with an on/off ratio up to 10^6 and ultralow leakage currents (10^{-13} A). Figure 4(c) shows I_{ds}–V_{ds} (I_{ds} and V_{ds} are the source-drain current and voltage, respectively) curves under dark and 255 nm laser illumination at different power intensities. An increase of I_{ds} is observed as the power density increase from 2.8×10^{-1} to 1.7×10^3 mW/cm^2, suggesting that the

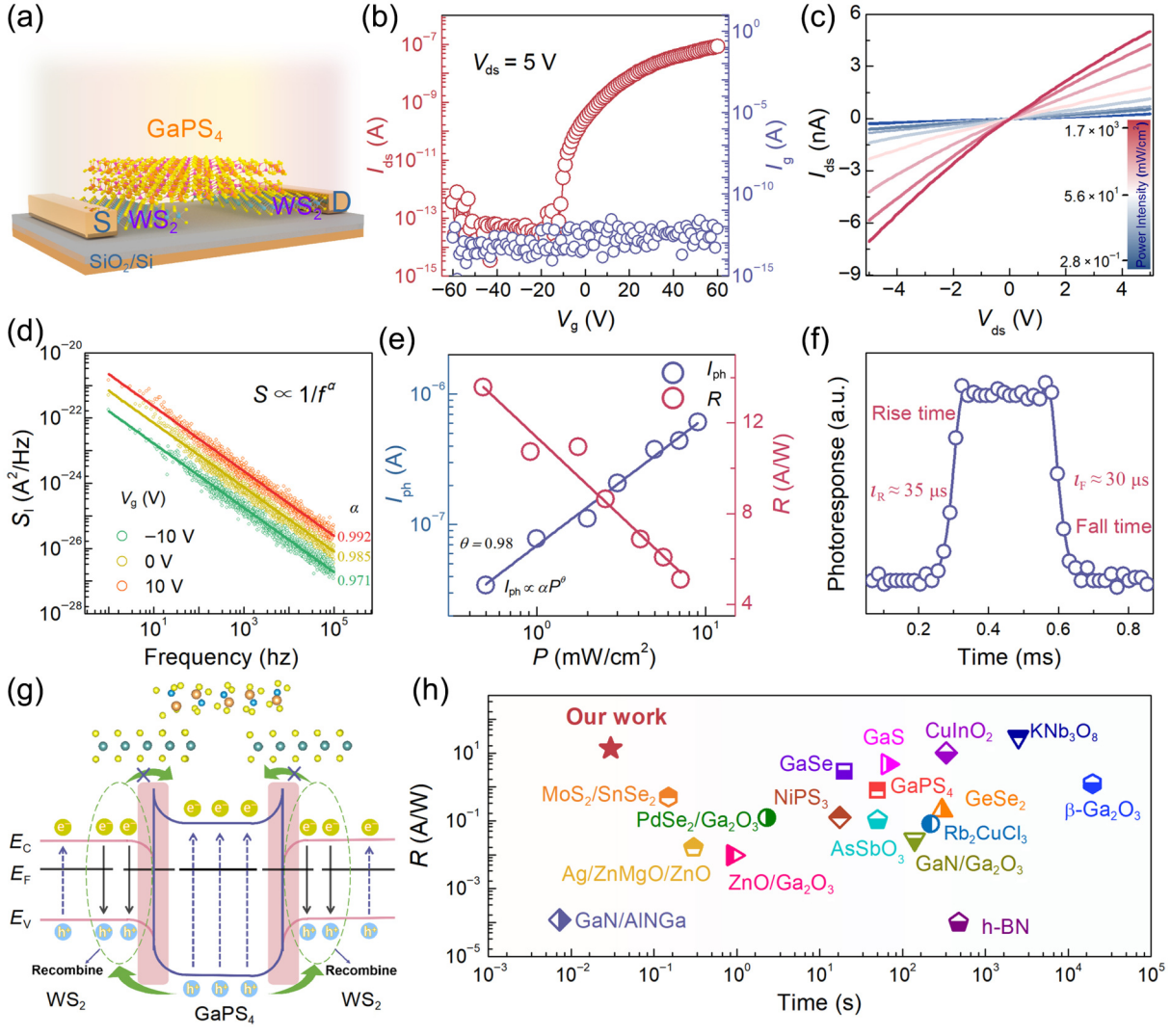

Figure 4 Photoelectric performance of $WS_2/GaPS_4$ dual-heterostructure photodetector. (a) Schematic illustration of $WS_2/GaPS_4$ dual-heterostructure device under illuminating with various wavelengths. (b) The representative plots of I_{ds} and leakage current (I_g) as function of V_g range from 60 to −60 V, implying high on/off ratios as 10^6 and low leakage currents (10^{-13} A). (c) I_{ds}–V_{ds} curves of $WS_2/GaPS_4$ dual-heterostructure device in the dark and under irradiation with different power density under 255 nm illuminations. (d) Noise spectral density of the device under different V_g at V_{ds} of 5 V. (e) Photoelectric performances metrics of I_{ph} and R as function of power intensity under 255 nm light illuminations. (f) Rise and fall time of $WS_2/GaPS_4$ dual-heterostructure device. (g) Energy band diagram illustrating the photodetection mechanism of the $WS_2/GaPS_4$ dual-heterostructure. (h) Comparison of response time and responsivity in the solar-blind UV photodetector based on other materials.

generation of photogenerated carriers is proportional to the number of absorbed incident photons [30]. Time-dependent photoresponse of $WS_2/GaPS_4$ dual-heterostructure photodetector under different power intensities and wavelengths of 255 and 360 nm is displayed in Figs. S14 and S15 in the ESM, indicating a stable photoresponse in solar-blind UV region. Moreover, the frequency-dependent noise spectral density (S_i) is shown in Fig. 4(d), which can be fitted by the equation $S_i \propto (1/f^{\alpha})$. The exponent α is calculated to be 0.971, 0.985, and 0.992 under gate voltages (V_g) of −10, 0, and 10 V, respectively, indicating that $1/f$ noise dominates the total noise of dual-heterostructure photodetector at low frequencies [31]. Figure 4(e) displays the photocurrent ($I_{ph} = I_{light} - I_{dark}$, where I_{light} and I_{dark} are the current under illumination and the dark current, respectively) and responsivity (R) as function of power intensity under 255 nm illumination. Notably, a nonlinear photoconductivity effect in $WS_2/GaPS_4$ dual-heterostructure photodetector is observed. Generally, I_{ph} can be fitted by the following equation: $I_{ph} \propto aP^{\theta}$, where a is a constant, P is laser power intensity, and θ is power factor ($\theta < 1$). The maximum I_{light}/I_{dark}, R, and external quantum efficiency (EQE) for the photodetector can be calculated as 3.6×10^3, 1.3×10^1 A/W, and 6.6×10^3% under 255 nm illumination, respectively (Figs. S16(a) and S16(b) in the ESM), which are higher than those of pure $GaPS_4$ [9], $WS_2/GaPS_4$ heterostructure (Fig. S17 in the ESM), GaSe [32], and ZnO-Ga_2O_3 [33]. As depicts in Fig. 4(f), the device exhibits the rise and fall time of 35 and 30 μs, respectively, which are attributable to the rapid separation of photocarriers and fast charge carrier transfer at the $WS_2/GaPS_4$ dual-heterostructure interface. Moreover, the photocurrent of $WS_2/GaPS_4$ dual-heterostructure photodetector shows no degradation after periodic on/off switching of the light for 10^4 cycles (Fig. S18 in the ESM), implying excellent durability and repeatability. Notably, the dual-heterostructure demonstrates remarkable operational stability across a wide temperature range from 163 to 473 K (Figs. S19 and S20, and Note S4 in the ESM). A comprehensive model with energy-band alignment is used to explain the mechanism underlying the nonlinear photocurrent behaviour (Fig. 4(g)). The $WS_2/GaPS_4/WS_2$ dual-heterostructure facilitates the efficient spatial separation of electron–hole pairs driven by the dual built-in electric fields. Here, $GaPS_4$ acts as a barrier layer, confining photogenerated carriers within the narrow-bandgap WS_2. Although holes flow unimpeded across the interface, electrons accumulate on the WS_2 side because of the potential barrier in the conduction band. This configuration significantly inhibits the electron–hole recombination and enhances the carrier collection efficiency, thereby boosting the photoelectric performance of the device. These results (Fig. 4(h)) highlight the superior performance of the $WS_2/GaPS_4$ dual-heterostructure photodetector compared to previously reported solar-blind UV photodetectors (see Table S1 in the ESM for a detailed comparison of merit values). Taking into consideration the ultra-low dark current, broad spectral sensitivity, and fast response time of the $WS_2/GaPS_4$ dual-heterostructure photodetector, its potential application in secure optical communications is explored through a photoelectric scanning system (see Fig. S21 and Note S3 in the ESM for details of optical communication application). Therefore, the outstanding performance of $WS_2/GaPS_4$ dual-heterostructure photodetector resulted in a strong double built-in electric field and high-spike barrier height, contributing to reduction in the recombination rate of electron–hole pairs and preventing electron transfer from WS_2 to $GaPS_4$.

The breaking of the interfacial symmetry between C_3-symmetric WS_2 and C_2-symmetric $GaPS_4$ substantially amplified the anisotropic optical absorption, endowing it with strong potential for polarization-sensitive solar-blind photodetection. As schematically depicted in Fig. 5(a), angle-resolved photocurrent measurements for the $WS_2/GaPS_4$ dual-heterostructure were performed using a continuously rotated half-wave plate positioned between a 255 nm light source and the device to sweep the linear-polarization vector. Time-resolved photoresponse curves (Fig. 5(b)) reveal the periodic modulation of the photocurrent ratio (I_{ph}/I_{dark}) with polarization angle. The polar-coordinates of the angle-dependent photocurrent (Fig. 5(c)) exhibit a pronounced two-lobed pattern. Consequently, the dichroic ratio (I_{max}/I_{min}) is calculated to be 3.4 under 255 nm illumination, which is higher than that of pristine $GaPS_4$ (1.85) and those of some other previously reported anisotropic materials in UV range, as summarized in Fig. 5(d). Benefiting from the ultralow dark current, the ultrafast response speed, and the high dichroic ratio, the polarization-resolved imaging capability of $WS_2/GaPS_4$ dual-heterostructure is evaluated using a single-pixel scanning system (Fig. 5(e)). A mask engraved with the "AHUMFMD" pattern (AnHui University, Magnetic Functional Materials and Device Laboratory, Fig. S22 in the ESM) was positioned between a half-wave plate and the detector, and its linear motion was controlled by an X–Y stage. The reconstructed "AHUMFMD" (61 pixels × 44 pixels) generated from polarization photocurrent data is displayed in Fig. 5(f). Each pixel within this matrix represents a specific polarization photocurrent intensity, which is assigned to corresponding color blocks. Using image processing techniques, these color blocks are combined to create the "AHUMFMD" image, while the computer records the photocurrent data. Figure 5(g) illustrates a schematic of the polarization imaging mechanism for calculating DoLP (see the detailed analysis in Section 2). The polarization images acquired at angles of 0°, 45°, 90°, and 135° are displayed in Fig. S23 in the ESM. The extracted imaging results of $WS_2/GaPS_4$ dual-heterostructure photodetector exhibit significantly enhanced contrast (Fig. 5(h)), demonstrating its exceptional polarization imaging capability.

4 Conclusions

The $WS_2/GaPS_4$ dual-heterostructure photodetector was successfully constructed by bridging the wide-bandgap semiconductor $GaPS_4$ in two adjacent n-type semiconductor WS_2 nanosheets. This unique design introduces a high electron barrier and a large built-in electric field at the $WS_2/GaPS_4$ dual-heterostructure interface, which not only ensures the efficient separation and transfer of photogenerated electron–hole pairs but also effectively suppresses the drift of minority carriers. In addition, the optical anisotropy of $WS_2/GaPS_4$ dual-heterostructure in the solar-blind UV region is significantly enhanced via symmetry-breaking engineering. The optoelectronic performance of $WS_2/GaPS_4$ dual-heterostructure photodetector in the solar-blind UV region exhibits a high R of 13.5 A/W, an EQE of 6.6×10^3%, and the photoresponse time of approximately 30 μs. Additionally, the in-plane optical anisotropy of the $WS_2/GaPS_4$ dual-heterostructure exhibits a high dichroic ratio up to 3.4 under 255 nm illumination. These results indicate that the $WS_2/GaPS_4$ dual-heterostructure device with polarization-imaging capabilities

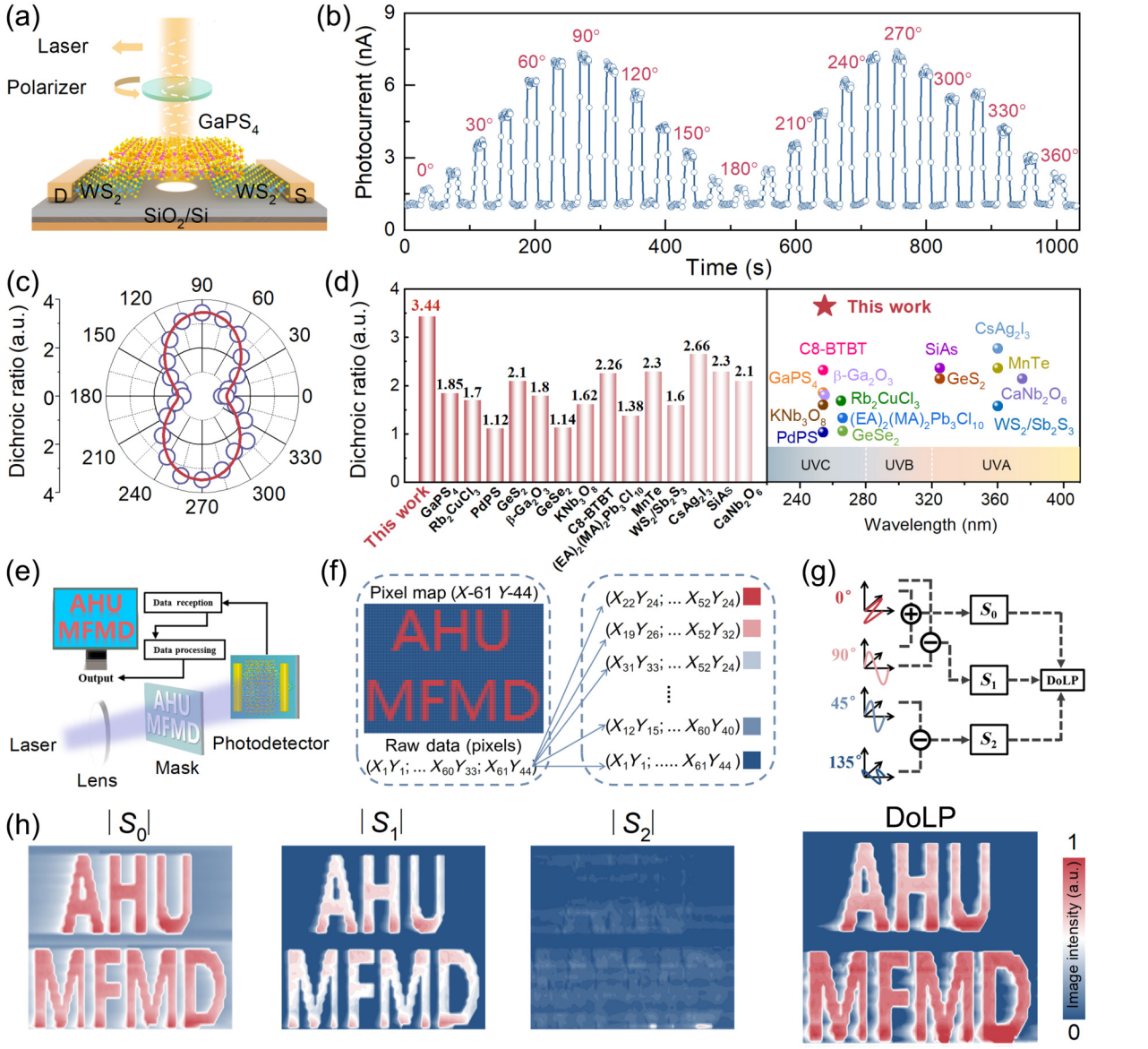

Figure 5 Polarized optoelectronic responses and polarization imaging applications of the $WS_2/GaPS_4$ dual-heterostructure device in solar-blind UV region. (a) The schematic view of $WS_2/GaPS_4$ dual-heterostructure polarized photodetection measurement. (b) Time-resolved photocurrent of $WS_2/GaPS_4$ dual-heterostructure device with different polarization angles with a 15° step under 255 nm illumination. (c) Plot of normalized dichroic ratio of the $WS_2/GaPS_4$ dual-heterostructure device. The DR is defined as $\frac{I_{ph,\ max}}{I_{ph,\ min}}$, where $I_{ph,max}$ and $I_{ph,min}$ represent the maximum and minimum photocurrents under polarization angles, respectively. (d) Photocurrent dichroic ratio comparison based on different materials, including $GaPS_4$ [9], KNb_3O_8 [10], Rb_2CuCl_3 [11], $(EA)_2(MA)_2Pb_3Cl_{10}$ [34], β-Ga_2O_3 [35], $GeSe_2$ [36], PdPS [37], C8-BTBT [38], GeS_2 [39], MnTe [40], WS_2/Sb_2S_3 [27], $CsAg_2I_3$ [41], SiAs [42], and $CaNb_2O_6$ [43]. (e) Schematic diagram of the measurement setup for an imaging sensor. (f) Real-time collection of raw photocurrent data and corresponding color mapping. (g) Schematic of the polarization imaging mechanism for the calculation of DoLP. (h) Imaging DoLP results for dual-heterojunction device using 255 nm laser illumination.

and polarization contrast enhancement has significant potential for applications in highly integrated electronics and optoelectronics in the solar-blind UV region.

Electronic Supplementary Material: Supplementary material (experimental and characterizations details) is available in the online version of this article at https://doi.org/10.26599/NR.2026.94908448.

Data availability

All data needed to support the conclusions in the paper are presented in the manuscript and the Electronic Supplementary Material. Additional data related to this paper may be requested from the corresponding author upon request.

Acknowledgements

This work was financially supported by the National Key Research and Development Program of China (No. 2022YFA1204000), the National Natural Science Foundation of China (Nos. 52571229, 52525207, 52130103, U21A2086, 52301226, and 52471248), Natural Science Foundation of Anhui Province (No. 2308085Y04), and Fundamental Research Program of Shanxi Province (No. 202403021222357).

Declaration of competing interest

All the contributing authors report no conflict of interests in this work.

Author contribution statement

Q. L., K. Y., and M. M. Y. designed the experiments, analyzed the data, and wrote the paper. J. X. Y., T. L. Z, and Q. L. grew the samples and fabricated the devices. K. Y., Y. H. G., Y. L., and B. H. conducted Raman, PL spectroscopy, and noise spectral measurements. Y. G., Q. G., and P. X. performed the XRD and AFM measurements. A. M. N and J. X. Y. carried out the TEM characterizations. Q. Q. Y., R. Q. C., and Z. F. S. helped with the TA spectroscopy test. K. Y. and Q. L. conducted photo-detection testing. Q. G. and W. Y. conducted DFT calculation. M. M. Y., W. Y., Z. Y. L., and S. G. W. contributed to the discussion and analysis of experimental data. All the authors have approved the final manuscript.

Use of AI statement

None.

References

[1] Bie, Y. Q.; Grosso, G.; Heuck, M.; Furchi, M. M.; Cao, Y.; Zheng, J. B.; Bunandar, D.; Navarro-Moratalla, E.; Zhou, L.; Efetov, D. K. et al. A $MoTe_2$-based light-emitting diode and photodetector for silicon photonic integrated circuits. *Nat. Nanotechnol.* **2017**, *12*, 1124–1129.

[2] Guo, D. Y.; Su, Y. L.; Shi, H. Z.; Li, P. G.; Zhao, N.; Ye, J. H.; Wang, S. L.; Liu, A. P.; Chen, Z. W.; Li, C. R. et al. Self-powered ultraviolet photodetector with superhigh photoresponsivity (3.05 A/W) based on the GaN/Sn:Ga_2O_3 pn junction. *ACS Nano* **2018**, *12*, 12827–12835.

[3] Zhu, T.; Su, J.; Alvarez, J.; Lefèvre, G.; Labat, F.; Ciofini, I.; Pauporté, T. Response enhancement of self-powered visible-blind UV photodetectors by nanostructured heterointerface engineering. *Adv. Funct. Mater.* **2019**, *29*, 1903981.

[4] Zeng, L. H.; Lin, S. H.; Li, Z. J.; Zhang, Z. X.; Zhang, T. F.; Xie, C.; Mak, C. H.; Chai, Y.; Lau, S. P.; Luo, L. B. et al. Fast, self-driven, air-stable, and broadband photodetector based on vertically aligned $PtSe_2$/GaAs heterojunction. *Adv. Funct. Mater.* **2018**, *28*, 1705970.

[5] Wang, Y. H.; Li, H. R.; Cao, J.; Shen, J. Y.; Zhang, Q. Y.; Yang, Y. T.; Dong, Z. G.; Zhou, T. H.; Zhang, Y.; Tang, W. H. et al. Ultrahigh gain solar blind avalanche photodetector using an amorphous Ga_2O_3-based heterojunction. *ACS Nano* **2021**, *15*, 16654–16663.

[6] Liu, B.; Chen, D. J.; Lu, H.; Tao, T.; Zhuang, Z.; Shao, Z. G.; Xu, W. Z.; Ge, H. X.; Zhi, T.; Ren, F. F. et al. Hybrid light emitters and UV solar-blind avalanche photodiodes based on III-nitride semiconductors. *Adv. Mater.* **2020**, *32*, 1904354.

[7] Lin, C. N.; Lu, Y. J.; Yang, X.; Tian, Y. Z.; Gao, C. J.; Sun, J. L.; Dong, L.; Zhong, F.; Hu, W. D.; Shan, C. X. Diamond-based all-carbon photodetectors for solar-blind imaging. *Adv. Opt. Mater.* **2018**, *6*, 1800068.

[8] Streicher, I.; Leone, S.; Zhang, M. L.; Tlemcani, T. S.; Bah, M.; Straňák, P.; Kirste, L.; Prescher, M.; Yassine, A.; Alquier, D. et al. Understanding interfaces in AlScN/GaN heterostructures. *Adv. Funct. Mater.* **2024**, *34*, 2403027.

[9] Yan, Y.; Yang, J. H.; Du, J.; Zhang, X. M.; Liu, Y. Y.; Xia, C. X.; Wei, Z. M. Cross-substitution promoted ultrawide bandgap up to 4.5 eV in a 2D semiconductor: Gallium thiophosphate. *Adv. Mater.* **2021**, *33*, 2008761.

[10] Ping, Y.; Long, H. R.; Liu, H.; Chen, C.; Zhang, N. N.; Jing, H. M.; Lu, J. B.; Zhao, Y. W.; Yang, Z. M.; Li, W. et al. Polarization sensitive solar-blind ultraviolet photodetectors based on ultrawide bandgap KNb_3O_8 nanobelt with fringe-like atomic lattice. *Adv. Funct. Mater.* **2022**, *32*, 2111673.

[11] Ma, J. L.; Zhang, M. Y.; Dun, C. H.; Ji, H. F.; Ma, Z. Z.; Chen, X.; Li, X. J.; Wu, D.; Shi, Z. F. Highly polarization-sensitive solar-blind ultraviolet photodetection based on 1D Rb_2CuCl_3 microwires. *Adv. Funct. Mater.* **2025**, *35*, 2414943.

[12] Yu, Y. L.; Xiong, T.; Zhou, Z. Q.; Liu, D. Y.; Liu, Y. Y.; Yang, J. H.; Wei, Z. M. Spectrum-dependent image convolutional processing via a two-dimensional polarization-sensitive photodetector. *Nano Lett.* **2024**, *24*, 6788–6796.

[13] Sang, K. R.; Wei, J. Y.; Han, W.; Chu, Z. Y.; Yuan, H.; Guo, C. G.; Liu, J. L.; Sun, Q. H.; Zeng, L. H.; Shen, L. P. et al. Enhanced linear dynamic range and response speed in interdigital-electrode solar-blind photodetector by contact engineering. *Appl. Phys. Rev.* **2025**, *12*, 021413.

[14] Sun, Q. H.; Han, W.; Liu, J. L.; Sang, K. R.; Jiang, J. X.; Wang, Z.; Wan, H. Z.; Zhang, J.; Wang, H. Improved response speed and detectivity of a solar-blind photodetector by contact engineering with an interdigital-electrode semimetal. *J. Mater. Chem. C* **2025**, *13*, 21908–21917.

[15] Han, W.; Wang, Z.; Guan, S.; Wei, J. Y.; Jiang, Y. R.; Zeng, L. H.; Shen, L. P.; Yang, D. H.; Wang, H. Recent advances of phase transition and ferroelectric device in two-dimensional In_2Se_3. *Appl. Phys. Rev.* **2024**, *11*, 021314.

[16] Wu, E. X.; Xie, Y.; Zhang, J.; Zhang, H.; Hu, X. D.; Liu, J.; Zhou, C. W.; Zhang, D. H. Dynamically controllable polarity modulation of $MoTe_2$ field-effect transistors through ultraviolet light and electrostatic activation. *Sci. Adv.* **2019**, *5*, eaav3430.

[17] Wu, E. X.; Xie, Y.; Liu, Q. Z.; Hu, X. D.; Liu, J.; Zhang, D. H.; Zhou, C. W. Photoinduced doping to enable tunable and high-performance anti-ambipolar $MoTe_2$/MoS_2 heterotransistors. *ACS Nano* **2019**, *13*, 5430–5438.

[18] Huo, S. D.; Meng, F. Y.; Zhang, Z.; Xie, Y.; Hu, X. D.; Wu, E. X. Bias voltage-switchable metal-insulator transition in 2D van der Waals TMDs FETs: Role of tunneling barriers. *Nano Res.* **2025**, *18*, 94907703.

[19] Yang, Z. Y.; Zhang, Z.; Huo, S. D.; Meng, F. Y.; Wang, Y.; Ma, Y. X.; Liu, B. Y.; Meng, F. Y.; Xie, Y.; Wu, E. X. Emerging 2D material-based synaptic devices: Principles, mechanisms, improvements, and applications. *SmartMat* **2025**, *6*, e70005.

[20] Du, M. C.; Huo, S. D.; Du, L. J.; Wang, Y. X.; Wu, E. X. Evidence of electron–phonon coupling in type-II Weyl semimetal $TaIrTe_4$. *Appl. Phys. Lett.* **2025**, *127*, 033101.

[21] Wang, J. Y.; Ling, C. C.; Xue, X.; Ji, H. G.; Rong, C.; Xue, Q. Z.; Zhou, P. H.; Wang, C. K.; Lu, H. P.; Liu, W. P. Self-powered and broadband photodetectors based on high-performance mixed dimensional Sb_2O_3/$PdTe_2$/Si heterojunction for multiplex environmental monitoring. *Small* **2024**, *20*, 2310107.

[22] An, K.; Pan, Y.; Rong, X. M.; Zheng, T.; Li, L.; Sun, H. R.; Zeng, J.; Sang, Y. H.; Huang, F. Y.; Yue, D. W. et al. High-performance self-driven polarization-sensitive imaging photodetectors based on fully depleted T-$MoSe_2$/GeSe/B-$MoSe_2$ van der Waals dual-heterojunction. *Adv. Funct. Mater.* **2024**, *34*, 2409331.

[23] Pan, Y. T.; Zhu, L. Q.; Lu, L. D.; Ou, J. Z.; Zhou, J. H.; An, C. H.; Dong, M. L. Polarized photodetectors based on 2D 2H-$MoTe_2$/1T′-$MoTe_2$/$MoSe_2$ van der Waals heterojunction. *Adv. Funct. Mater.* **2024**, *34*, 2407931.

[24] Li, Y.; Zhang, C.; Zhuang, T. T.; Lin, Y.; Tian, J.; Qi, X. Y.; Li, X. F.; Wang, R.; Wu, L.; Liu, G. Q. et al. One-dimensional superlattice heterostructure library. *J. Am. Chem. Soc.* **2021**, *143*, 7013–7020.

[25] Wang, Z. H.; Zhang, H.; Wang, W. K.; Tan, C. Y.; Chen, J. W.; Yin, S. Q.; Zhang, H. L.; Zhu, A. K.; Li, G.; Du, Y. C. et al. Type-I heterostructure based on WS_2/PtS_2 for high-performance photodetectors. *ACS Appl. Mater. Interfaces* **2022**, *14*, 37926–37936.

[26] Ye, K.; Liu, L. X.; Liu, Y. J.; Nie, A. M.; Zhai, K.; Xiang, J. Y.;

Wang, B. C.; Wen, F. S.; Mu, C. P.; Zhao, Z. S. et al. Lateral bilayer MoS_2–WS_2 heterostructure photodetectors with high responsivity and detectivity. *Adv. Opt. Mater.* **2019**, *7*, 1900815.

[27] Ye, K.; Yan, J. X.; Li, Q.; Wang, L. Y.; Gao, Y.; Wang, L. M.; Zhang, F.; Jia, Z. Y.; Liu, L. X.; Nie, A. M. et al. Symmetry breaking in twisted mixed-dimensional heterostructure interfaces for multifunctional polarization-sensitive photodetection. *ACS Nano* **2025**, *19*, 1340–1351.

[28] Liu, Q. R.; Wei, K.; Tang, Y. X.; Xu, Z. J.; Cheng, X. A.; Jiang, T. Visualizing hot-carrier expansion and cascaded transport in WS_2 by ultrafast transient absorption microscopy. *Adv. Sci.* **2022**, *9*, 2105746.

[29] Chen, J. Y.; Xie, X.; Oyang, X.; Li, S. F.; He, J.; Liu, Z. W.; Wang, J. T.; Liu, Y. P. Giant optical anisotropy induced by magnetic order in $FePS_3$/WSe_2 heterostructures. *Small* **2024**, *20*, 2404346.

[30] Jia, Z. Y.; Xiang, J. Y.; Wen, F. S.; Yang, R. L.; Hao, C. X.; Liu, Z. Y. Enhanced photoresponse of SnSe-nanocrystals-decorated WS_2 monolayer phototransistor. *ACS Appl. Mater. Interfaces* **2016**, *8*, 4781–4788.

[31] Zeng, Z. X. S.; Sun, X. X.; Zhang, D. L.; Zheng, W. H.; Fan, X. P.; He, M.; Xu, T.; Sun, L. T.; Wang, X.; Pan, A. L. Controlled vapor growth and nonlinear optical applications of large-area 3R phase WS_2 and WSe_2 atomic layers. *Adv. Funct. Mater.* **2019**, *29*, 1806874.

[32] Hu, P. G.; Wen, Z. Z.; Wang, L. F.; Tan, P. H.; Xiao, K. Synthesis of few-layer GaSe nanosheets for high performance photodetectors. *ACS Nano* **2012**, *6*, 5988–5994.

[33] Zhao, B.; Wang, F.; Chen, H. Y.; Zheng, L. X.; Su, L. X.; Zhao, D. X.; Fang, X. S. An ultrahigh responsivity (9.7 $mA{\cdot}W^{-1}$) self-powered solar-blind photodetector based on individual ZnO–Ga_2O_3 heterostructures. *Adv. Funct. Mater.* **2017**, *27*, 1700264.

[34] Xu, Z. Y.; Weng, W.; Li, Y. B.; Liu, X. T.; Yang, T.; Li, M. F.; Huang, X. Y.; Luo, J. H.; Sun, Z. H. 3D-to-2D dimensional reduction for exploiting a multilayered perovskite ferroelectric toward polarized-light detection in the solar-blind ultraviolet region. *Angew. Chem., Int. Ed.* **2020**, *59*, 21693–21697.

[35] Li, L.; Yan, S. H.; Ma, W. Y.; Zhang, J. H.; Zhang, S. H.; Jiang, M. M.; Gao, L. F.; Tang, W. H.; Liu, Z. Angle-resolved polarization Raman spectroscopy of β-Ga_2O_3 and their application in sensitive solar-blind photodetection. *Appl. Phys. Lett.* **2024**, *125*, 141102.

[36] Yan, Y.; Xiong, W. Q.; Li, S. S.; Zhao, K.; Wang, X. T.; Su, J.; Song, X. H.; Li, X. P.; Zhang, S.; Yang, H. et al. Direct wide bandgap 2D $GeSe_2$ monolayer toward anisotropic UV photodetection. *Adv. Opt. Mater.* **2019**, *7*, 1900622.

[37] Wang, X. G.; Xiong, T.; Zhao, K.; Zhou, Z. Q.; Xin, K. Y.; Deng, H. X.; Kang, J.; Yang, J. H.; Liu, Y. Y.; Wei, Z. M. Polarimetric image sensor and Fermi level shifting induced multichannel transition based on 2D PdPS. *Adv. Mater.* **2022**, *34*, 2107206.

[38] Chen, S. N.; Liu, Z. X.; Long, H. R.; Yang, J. X.; Li, Z.; Cai, Z. R.; Qu, Z. Y.; Shao, L. J.; Shi, X. S.; Jiang, L. et al. A general vapor-induced coating approach for layer-controlled organic single crystals. *Adv. Funct. Mater.* **2023**, *33*, 2212158.

[39] Yang, Y. S.; Liu, S. C.; Wang, X.; Li, Z. B.; Zhang, Y.; Zhang, G. M.; Xue, D. J.; Hu, J. S. Polarization-sensitive ultraviolet photodetection of anisotropic 2D GeS_2. *Adv. Funct. Mater.* **2019**, *29*, 1900411.

[40] Ye, K.; Yan, J. X.; Liu, L. X.; Li, P. H.; Yu, Z. P.; Gao, Y.; Yang, M. M.; Huang, H.; Nie, A. M.; Shu, Y. et al. Broadband polarization-sensitive photodetection of magnetic semiconducting MnTe nanoribbons. *Small* **2023**, *19*, 2300246.

[41] Yu, M. X.; Zhai, Y. L.; Xu, K.; Song, R. J.; Wan, P.; Shi, D. N.; Kan, C. X.; Fang, X. S.; Jiang, M. M. CVD-synthesized $CsAg_2I_3$ single crystals toward polarization UV photodetection and anti-counterfeiting identification. *Adv. Funct. Mater.* **2025**, *35*, 2413903.

[42] Kim, D.; Park, K.; Lee, J. H.; Kwon, I. S.; Kwak, I. H.; Park, J. Anisotropic 2D SiAs for high-performance UV–visible photodetectors. *Small* **2021**, *17*, 2006310.

[43] Qin, J. K.; Xiao, H.; Zhu, C. Y.; Zhen, L.; Xu, C. Y. Low-symmetry 2D perovskite $CaNb_2O_6$ for polarization-sensitive UV photodetection. *Adv. Opt. Mater.* **2022**, *10*, 2201627.